Broadband graded index Gutman lens with a wide field of view utilizing artificial dielectrics

Research Article | Vol. 28, No. 10 / 11 May 2020 / Optics Express 14648
Optics EXPRESS

Broadband graded index Gutman lens with a wide field of view utilizing artificial dielectrics: a design methodology

PETROS BANTAVIS,[1,2,*] CEBRIAN GARCIA GONZALEZ,[1] RONAN SAULEAU,[2] GEORGE GOUSSETIS,[3] SEGOLENE TUBAU,[4] AND HERVE LEGAY[4]

[1]*Research and Development, Idonial, Gijon, Spain*
[2]*Univ Rennes, CNRS, IETR (Institut d'Électronique et de Télécommunications de Rennes), - UMR 6164, F-35000 Rennes, France*
[3]*Institute of Sensors, Signals and Systems, Heriot-Watt University, Edinburgh dr38, UK*
[4]*Research and Technology Department, Thales Alenia Space, Toulouse, France*
[*]*petros.bantavis@univ-rennes1.fr*

Abstract: A novel all-metal graded index Gutman lens is proposed. It exploits an interleaved metasurface unit-cell with glide symmetry that can provide high values of equivalent refractive index with low frequency dispersion. The result is a compact lens with broadband performance and a wide field of view up to $\pm 70^{\circ}$. The proposed lens exhibits low loss, directive beams and is an appealing candidate for space applications. The design approach introduced can be applied to other graded index lenses with circular symmetry using rectangular or circular periodic structures.

1. Introduction

Lenses have been used for a wide range of applications such as radars, medical systems, space applications, acoustics, plasmonics and optics. Luneburg lenses, firstly introduced in [1], have been studied extensively because of their superior performance in terms of spherical aberrations in relation to beam scanning. In particular, the radiated beam can be scanned over a wide field of view by displacing the feed mechanically along the lens periphery. However, Luneburg lenses call for materials that can provide graded index (GRIN) of refraction, which make their implementation complicated. To overcome such challenges, Luneburg lenses utilizing metasurfaces or metamaterials have been implemented [2]. This approach provides more flexibility as the index variation along the lens surface can be controlled by modulating the geometry of an otherwise periodic structure. The latter can lead to a simplified manufacturing process and potentially also to reduced mass. 2D and 3D GRIN Luneburg lenses have been largely implemented using various periodic structures for a wide range of applications from microwave to optical frequencies [3–7] including in plasmonics. For example, in [8] electron beam lithography has been used to fabricate a plasmonic Luneburg lens based on holes in a dielectric thin film. Luneburg lenses have also inspired various types of integrated photonic circuits such as waveguide tapers [9] and couplers [10].

For antenna applications in the microwave and mm-wave range, the bulkiness of traditional Luneburg lenses can be a disadvantage. An approach to reduce the physical volume of quasi-optical devices with media with variable refractive indices has been introduced in [11] and [12] and is referred to transformation optics (TO). This method exploits coordinate transformations between the initial reference mesh and a transformed mesh, which enables the calculation of new values of permittivity and permeability for the transformed design that leads to similar performance behaviour as the reference one [13]. This class of transformation techniques has been applied to design new lenses [14–17], including evolutions of the Luneburg lens towards

#389887 https://doi.org/10.1364/OE.389887
Journal © 2020 Received 6 Feb 2020; revised 31 Mar 2020; accepted 1 Apr 2020; published 29 Apr 2020

Optics EXPRESS

more compact designs [18,19]. In these works, a curved part of the focal surface of the Luneburg is transformed into a planar surface. The planar transformed surface of the new lens enables the integration of traditional planar feeds such as phased array configurations. However, these transformed lenses call for high values of refractive index, which can be difficult to implement. An alternative design consists in using materials that can be found in nature [20,21]. However, as mentioned above, such approaches lead to more complex and less flexible designs.

An alternative transformation technique to reduce the volume of the traditional Luneburg lens has been presented by [22]. An asset of this radiator is that the focal point can be placed closer to the center of the lens and thus leading to a more compact lens. It can be proven that, similar to the Luneburg lens, the Gutman lens is free of spherical aberrations and achieves similar radiation performance [22]. A first implementation of this type of lens has been presented in [23] where a Gutman lens with wide scan and broadband performance has been synthesized by multiple dielectric layers. In [24] a 3D GRIN Gutman lens has been designed and tested using additive manufacturing utilizing a dielectric cubic periodic cell. However, in both configurations a planar surface approximation of the lens is selected and resulted on aberrations for the offset beams.

All-metal periodic structures in a parallel plate waveguide (PPW) technology have been extensively analysed in [25] where it is demonstrated that double-pin structures in a glide symmetry topology, and especially when interleaved, can provide artificial dielectrics with high index values and lower frequency dispersion in comparison with the single pin unit-cells. For instance, in [26] a horn lens is designed using the glide symmetry cell in gap waveguide technology where very low dispersion is achieved using the double-pin unit-cell. In [27] a Luneburg lens has been implemented using a glide symmetry unit-cell at Ka-band and resulted on a lens with wide field of view up to ±50°. Moreover, the glide index cell has been applied to design transformed lenses where high index values are needed. In [28] this cell is used to form a very compact transformed lens. A new degree of freedom (DoF) of the double-pin topology glide symmetry cell consists in interleaving topology of the top and bottom pins of the PPW. This DoF can lead to even higher index values with low dispersion and this will be further discussed in section 2.2.2.

In this work, a mm-wave 2D GRIN Gutman lens in an all-metal PPW implementation is introduced, which can be of relevance in e.g. multi-beam satellite missions. The novelty of the manuscript is twofold. First the GRIN Gutman lens that is presented uses all-metal artificial dielectrics, thereby avoiding dielectric losses while simplifying manufacturing. Additionally, the proposed design provides a wide field of view free of spherical aberrations while maintaining a compact size. A design methodology is presented which can be applied to every all-metal GRIN lens with circular symmetry in a PPW technology. The manuscript is organised as follows. The operation of the Gutman lens is presented in Section 2 together with the design methodology for synthesizing the lens. The lens performance is reported in Section 3. Conclusions are then drawn in section 4.

2. Design methodology

2.1. Description of the GRIN Gutman lens

The Gutman lens is introduced in [22] as a modified Luneburg lens. It has the same dimensions as the Luneburg lens, however the excitation source can be moved in smaller focal circles. This, in turn, enables accommodating the feed network within the area that would otherwise be occupied by a Luneburg lens. To calculate the required permittivity values along the surface of the lens, Hamiltonian transformation optics are applied to the Luneburg lens based on ray tracing. The corresponding distribution of the lens relative permittivity is provided by Eq. (1) where f is the

Optics EXPRESS

focal distance, R the radius of the lens and r the spatial position from the origin.

$$\epsilon_r = \frac{1 + \left(\frac{f}{R}\right)^2 - \left(\frac{r}{R}\right)^2}{\left(\frac{f}{R}\right)^2} \tag{1}$$

Based on Eq. (1), smaller focal distance f (focal circles) is associated with higher permittivity values, ϵ_r, and therefore higher values for the effective index of refraction, n_{eff}, since the latter is related to the dielectric permittivity according to $n_{eff} = \sqrt{\epsilon_r}$. For the Luneburg lens, which is obtained at the limit $f = R$, the index distribution along the lens varies from n_{eff}=1 to n_{eff}=1.4. However, since smaller focal circles are selected, the required index varies and higher index values are required to synthesize the lens. For instance, for a focal circle $f = R/2$, the index values varies from n_{eff}=1 to n_{eff}=2.2 (see Fig. 1(a)) and for $f = R/3$ the index values varies from n_{eff}=1 to n_{eff}=3.1.

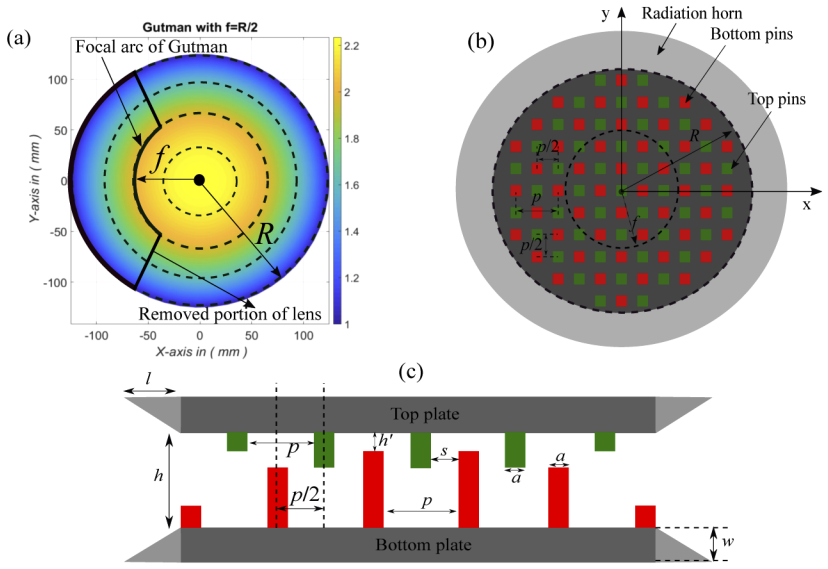

Fig. 1. (a) Effective refractive index n_{eff} of the Gutman Lens with focal arc $f = R/2$, (b) PPW GRIN Gutman lens layout using an IGS unit cell (top view), (c) 2D cut view, p=2.4, a=0.8, s=0.4, h'=1.9, h=4, w=12, all dimensions in mm.

In this work, we employ an example of a Gutman lens with focal circle $f = R/2$. To synthesize the lens, modulated periodic structures comprised of metal pins in a PPW housing are utilized as depicted in Fig. 1(b) and Fig. 1(c). Achieving a range that covers the highest required index n_{eff}=2.2 with low dispersion is therefore requested to implement a lens with stable performance across the entire Ku-band. An interleaved unit-cell has been selected to modulate the required indices along the surface of the lens. This type of cell is an artificial periodic structure and will be extensively analysed in section 2.2.

In order to provide efficient matching of the fields travelling from the feed to the edge of the lens such that they can radiate into free space, a radiation horn flare is accommodated along the periphery of the lens (see Fig. 1(b) and Fig. 1(c)). The excitation sources along the focal arc of the lens are accommodated by virtue of removing a portion of the lens (see Fig. 1(a)). This allows for increased compactness compared to the traditional Luneburg lens. Since the feeds are placed along a focal circle that is smaller than the radius of the lens R, at their interface with the

Optics EXPRESS

lens they experience an effective index of refraction larger than unity. Consequently, impedance matching for the excitation feeds needs also to be addressed.

2.2. Interleaved glide symmetry unit cell

The maximum index value of the considered Gutman lens is n_{eff}=2.2 (at its center, r= 0). It defines the highest value for the effective index of refraction that the artificial dielectric should provide. For operation of the lens across a wide bandwidth, low frequency dispersion of the artificial dielectric is also required. Glide symmetry double-pin all-metal structures in a PPW [29] provide favourably high effective index values with low dispersion. As discussed next, an interleaved glide symmetry (IGS) unit-cell is introduced here that results in maximum index values up to n_{eff}=2.2 with dispersion stability ±0.05 across the entire Ku-band.

We commence by defining the PPW height, which in Fig. 2(a) is noted as h. In particular, in order to avoid higher order modes the PPW height should be selected to be less than $\lambda/2$ where λ is the free space wavelength at the highest operating frequency. Otherwise, larger values are preferred in terms of ohmic losses and manufacturing tolerances. In the example considered here we therefore define h=4 mm. We next select the dimensions of the square unit-cell, which in Fig. 2(a) is marked as p. Lower values provide closer approximation to an artificial dielectric but increased ohmic losses, reduced design flexibility as well as more demanding manufacturing tolerances. Here we select p=2.4 mm, which corresponds to $\lambda/10$ at center frequency f = 12.5 GHz.

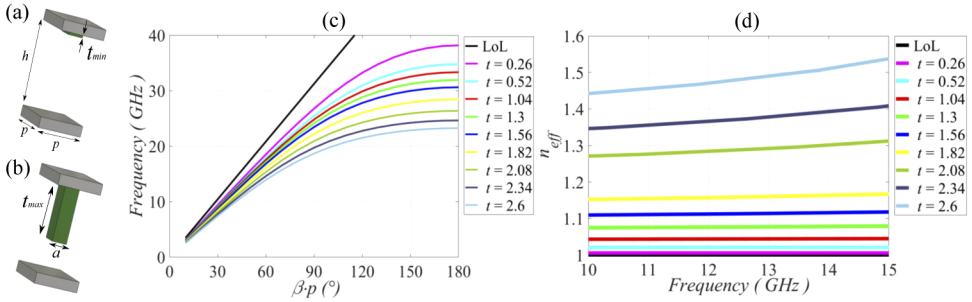

Fig. 2. (a) LoL propoagation (b) fakir unit cell - first DoF (c) dispersion and (d) effective index values.

Once periodicity is introduced in the PPW housing by means of the pins, the phase velocity of the propagating mode is reduced [30], leading to an increase of the effective index of refraction. In order to calculate the effective index of refraction associated with the unit-cell, full wave electromagnetic simulations are conducted using CST Microwave Studio. Periodic boundary conditions are applied to the unit-cell along the tangential plane with an appropriate phase shift imposed across opposing sides that corresponds to the propagation constant, β. The frequency associated with the given propagation constant is the calculated by means of an eigenmode solution. Repeating the process for the range of propagation constants, β, along the irreducible Brillouin zone provides the dispersion curve associated with the unit-cell. Finally, the equivalent effective index n_{eff} is derived from $n_{eff} = c\beta/2\pi f$.

We next study the effective index of refraction as a function of the geometrical parameters of the unit-cell. In order to reduce the geometrical degrees of freedom, we fix the cross sectional edge of the pins to a suitable value in light of the unit-cell dimensions, here at a=0.8 mm. With reference to Fig. 2(a), we then study the impact of the height, t, of the top metal post (green post in Fig. 2(b)) on the equivalent index of refraction. Simulated dispersion curves and extracted effective index of refraction are depicted in Fig. 2(c) and Fig. 2(d).

Optics EXPRESS

The minimum height of the cell is t_{min}=0 mm and in the absence of lower pins, this leads to a uniform PPW. The latter supports a pure TEM mode with dispersion coinciding with the line of light (LoL) and hence an equivalent index of refraction n_{eff}=1. For large values of the pin height, t, that approach the PPW height, h, high dispersion is observed. Thus, the maximum height of the pin is selected at t=2.6 mm leading to n_{eff}=1.48, Fig. 2(d).

Another degree of freedom arises from the metal posts on the bottom part of the PPW section placed in a glided symmetry position, Fig. 3(a) where g varies from g=0 mm to g=1.2 mm. The last DoF is the interleaving between the top and bottom metal posts, Fig. 3(b) where g varies from g=1.2 mm to g=2.09 mm (s=a/2). Simulated dispersion curves obtained for a fixed height of the top metal post at t=2.6 mm and associated extracted effective index of refraction is depicted in Fig. 3(c) and Fig. 3(d). As shown, varying the height g of the bottom post (red posts) from g=0 mm to g=1.2 mm leads to an increasing index of refraction up to n_{eff}=1.8. Then, from g>1.2 mm to g=2.09 mm the metal posts of the top and bottom plate are interleaved and lead to maximum index of n_{eff}=2.2. In conclusion, the combination of the fakir bed of nails and the interleaved glide symmetry cell lead to an index coverage from n_{eff}=1 to n_{eff}=2.2 and the unit-cell can be utilized to synthesize the Gutman lens.

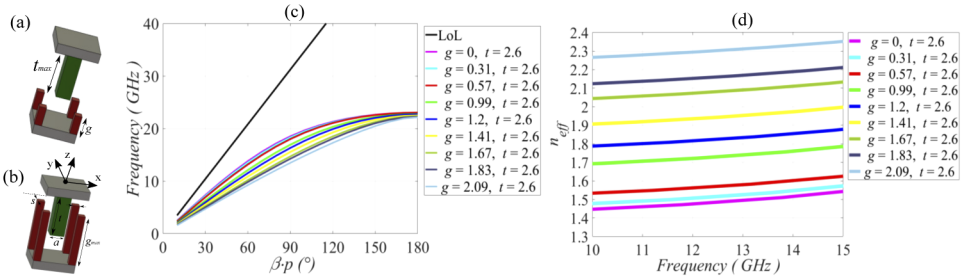

Fig. 3. (a) Glide symmetry cell without interleaving (b) Glide symmetry cell with interleaving (c) dispersion and (d) effective index values.

2.2.1. Misalignments

A parametric study on the misalignments of the bottom and top pins is valuable to evaluate the impact of manufacturing imperfections. Here the sensitivity of the refractive index value is studied for its nominal maximum value of n_{eff}=2.2 associated with the dimensions g=1.9 mm and t=2.6 mm. On one parametric setup, the top pin is shifted through the diagonal direction (see Fig. 4(a)). For the maximum shifted value of a=0.2 mm, the index increases and the dispersion of the cell slightly increases.

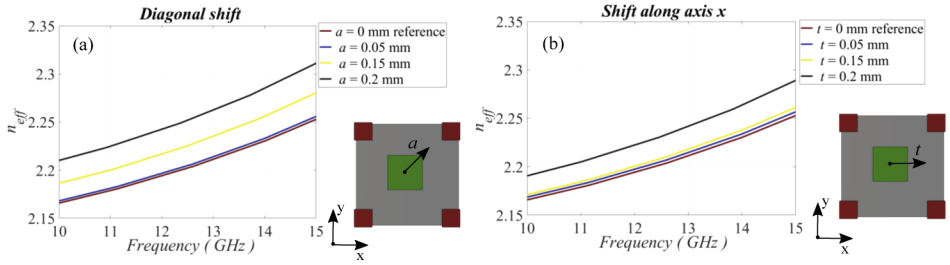

Fig. 4. Parametric study on the misalignments of the interleaved unit-cell (a) top pin diagonal shifting (b) top pin shifting along axis x .

Optics EXPRESS

On another parametric setup, the top pin is shifted through axis x (see Fig. 4(b)). On this configuration the impact of the shifting position of the cell on its index values is not significant in comparison with the diagonal shifting, except for the extreme shifting value of t=0.2 mm.

2.2.2. High index unit cells

As discussed in section 2.2, the unit-cell with interleaved pins and glide symmetry can accommodate for effective index values that reach n_{eff}=2.2 required in the Gutman lens design. In order to complete the study towards even higher values and further confirm the choice of the selected glided symmetry cell, this section presents additional studies. In particular, we study the selected unit-cell against its variant where the top and bottom pins do not interleave as well as a unit-cell with a single pin. Results presented in Fig. 5(a) indicate that the refractive index value n_{eff}=1.4 of the single pin fakir unit-cell leads to high dispersion at Ku-band, while the double-pin cell with glide symmetry and no interleaving between the top and the bottom pins [26], reduces the dispersion. This is in agreement with the conclusions of [25] where the double-pin cell in a glide symmetry topology is less dispersive compared to the single pin unit-cell.

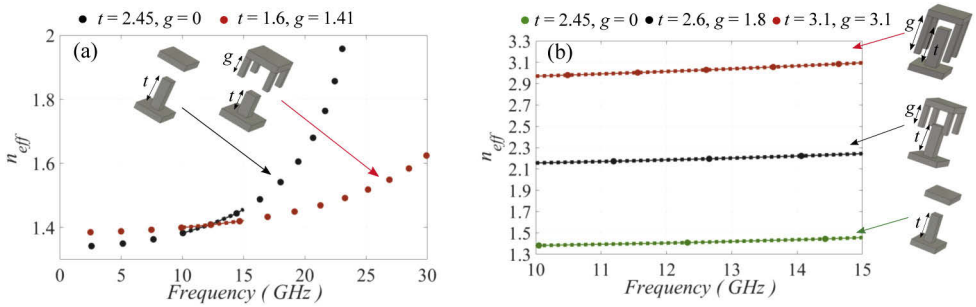

Fig. 5. Index comparison of (a) single pin unit-cell vs glide symmetry cell without interleaving (b) single pin unit cell vs glide symmetry cell with slight interleaving vs glide symmetry cell with maximum interleaving.

Figure 5(a) further indicates that higher values of the effective index of refraction for these unit-cells lead to high dispersion that can be impractical for lens applications. In contrast, the selected unit-cell leads to significantly lower dispersion even for higher values of the effective index of refraction. For instance, in Fig. 5(b) the interleaved double-pin glide symmetry cell with dimensions t=2.6 mm and g=1.8 mm shows maximum index value n_{eff}=2.2 with very low dispersion compared to the maximum value of the single pin cell. Moreover, if the height of the top and bottom pins increases (t=3.1 mm, g=3.1), a maximum value of n_{eff}=3 is reached with low dispersion.

2.3. Synthesizing the lens

Following the methodology described in section 2.2 a map of geometrical dimensions to effective index of refraction is obtained. The next step is the definition of the geometrical dimensions to synthesize the lens. At this point, a design methodology is proposed which can be applied in every GRIN lens which has circular symmetry utilizing metal posts. The goal of the design is to place the relevant metal posts of both top and bottom plates which represent the equivalent indices of the Gutman lens along its surface.

The first design step is the discretization of the lens and is depicted in Fig. 6(a). While the radius of the lens is equal to R=125 mm and the periodicity of the unit-cell is p=2.4 mm, for $x \in A$, where $A = \{0, R\}$ the discretization gives K=R/p=52 cells. Via exploiting the circular symmetry of the lens, the analysis of the discretization can converge upon the area $A = \{X, Y\}$ where

Optics EXPRESS

$X = \{0, R\}$ and $Y = \{-a/2, a/2\}$. Also, the design analysis can focus on the discretized data which correspond to the to the n_{eff} values on the area $A = \{X, Y\}$ and are approximately depicted in Fig. 6(b). For $x \in A$, each interleaved glide symmetry unit-cell represents K discretized n_{eff} values.

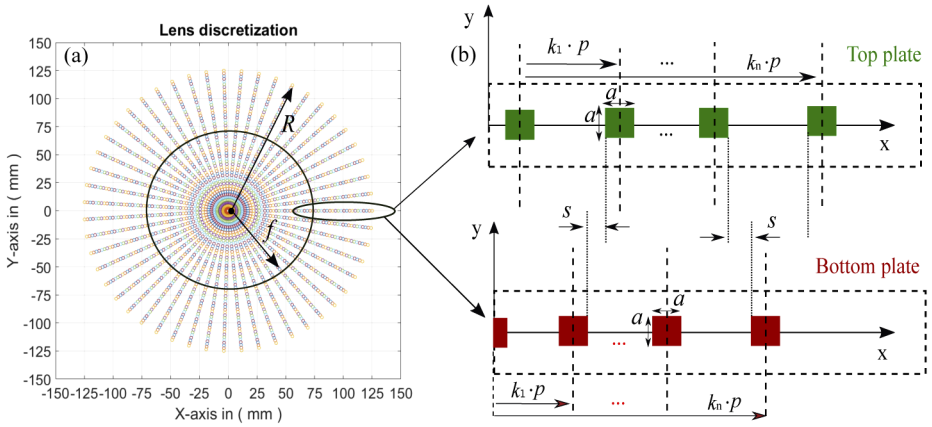

Fig. 6. (a) Lens discretization, (b) K discretized values of the bottom and top metal posts.

The next step is to extract index values from the dispersion graphs that have been calculated and depicted in Fig. 2(d) and Fig. 3(d). For $x \in A$ based on Eq. (1), the index distribution of the Gutman lens is depicted in Fig. 7(a). Based on the dispersion study of the previous section, the top and bottom metal posts need to be placed in the whole surface of the lens to mimic the required indices of Fig. 7(a). As it is depicted in Fig. 7(b) the fakir bed of nails cell covers only the area which can be represented by $A_{fakir(cell)}$=K_n-K_{42}=10 discretized values. These 10 discetized data represent the index range $1<n_{eff}<1.48$. Thus, 10 index values are extracted from the fakir unit-cell and are depicted in Fig. 8(a). Then, for the rest area until the center of the lens, the glide symmetry cell is placed and $A_{glide(cell)}$=K_{42}-0=42 index values are extracted and they are depicted in Fig. 8(b). These 42 discretized data represent the index range $1.48<n_{eff}<2.25$. As a result, the required database for the calculation of the equivalent heights of the metal posts on the surface of the lens is formed.

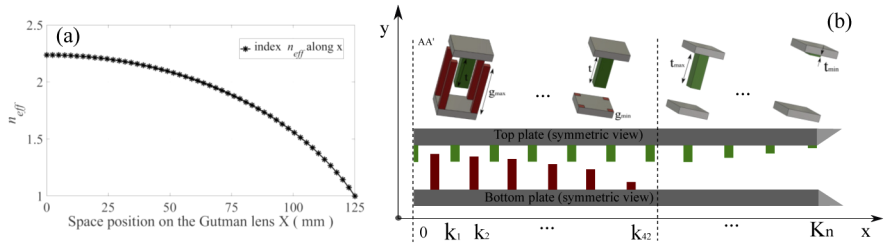

Fig. 7. (a) Required effective index values of the Gutman lens for $x \in A$, (b) unit-cell design stages to form the required indices.

In the process of exploiting the circular symmetry of the lens, the next step is the design of a $K \times K$ matrix with K= 52 rectangular metal posts of equal heights. This matrix is the quarter part of the full lens matrix surface that is depicted in Fig. 9(a). The index values of the quarter part of the matrix are depicted in Fig. 9(b) and its 3D view in Fig. 9(c). It is composed of $K \times K$ rectangular metal posts with post width a=0.8 mm and periodicity p=2.4 mm. The height of

Optics EXPRESS

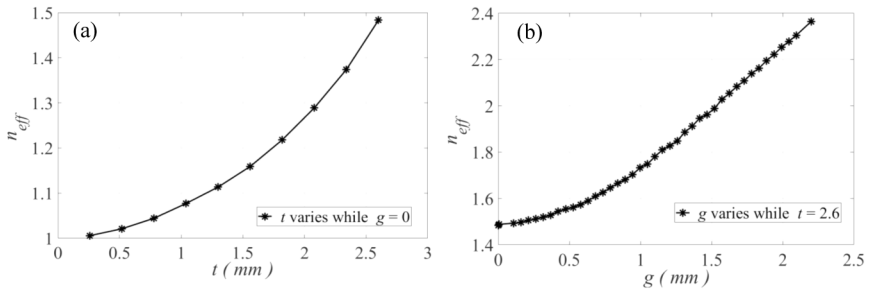

Fig. 8. (a) Extracted index data from the dispersion of the fakir cell, (b) extracted index data from the dispersion of the glide symmetry cell.

the posts is equal to h=2.1 mm and it is located through axis z. This is the maximum height of the metal post on the bottom part of the lens and taking into account the dispersion study of the previous section it is settled on the center of the lens. The metal posts are placed on the surface of a circle which represents the bottom PPW plate and has a radius equal to R=125 mm.

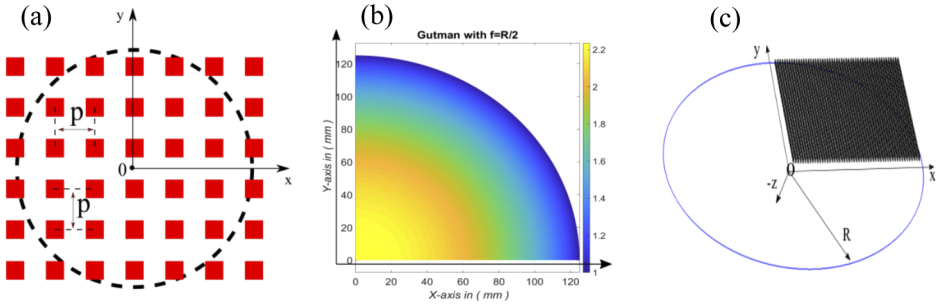

Fig. 9. (a) $K \times K$ matrix designed for bottom metal pins with equal heights h, top view (b) index distribution along its quarter symmetric surface (c) 3D $K \times K$ matrix with equal height bottom metal plates.

The final step is to calculate the required heights of the metal posts based on the dispersion data calculated on the previous section. The index values n_{eff} along the axis X of the lens is known for all the discretized positions from Fig. 8(a) and Fig. 8(b). The index values n_{eff} for $A_{glide(cell)}$=42 discretized heights g of the bottom metal posts are known and are depicted in Fig. 8(b). Thus, by utilizing data extrapolation the values of Fig. 7(a) and Fig. 8(b), the bottom post heights g along the axis X of the lens are computed and are shown in Fig. 10(a). For the rest 10 discretized values, the data vector is filled with zeros as the height of the bottom metal plate is g=0 mm. Thus, the height of the bottom metal posts has been calculated. The same procedure has been applied for the calculation of the top plate heights and their heights are depicted in Fig. 10(b).

Through extracting the data of Fig. 10(a) and Fig. 10(b), two 2D splines (one spline for the bottom and a second for the top plate pins) are designed and imported to the $K \times K$ matrix that was designed with equal heights g of the bottom metal posts. For instance, in Fig. 11(a) the bottom plate pins with equal heights are depicted. The 2D spline with the data of Fig. 10(a) is imported and then was reproduced, rotated by 5° to create a surface. This surface represents the modulation of the bottom pins of the PPW. A 2D view is also depicted in Fig. 11(b). The elements that were out of the range of this surface were removed and the expected height of the bottom pins of Fig. 10(a) is reached. The final modulated metal posts are depicted in Fig. 11(c) where the pins are detached on the bottom circular metal plate of the PPW. The rest posts of the

Optics EXPRESS

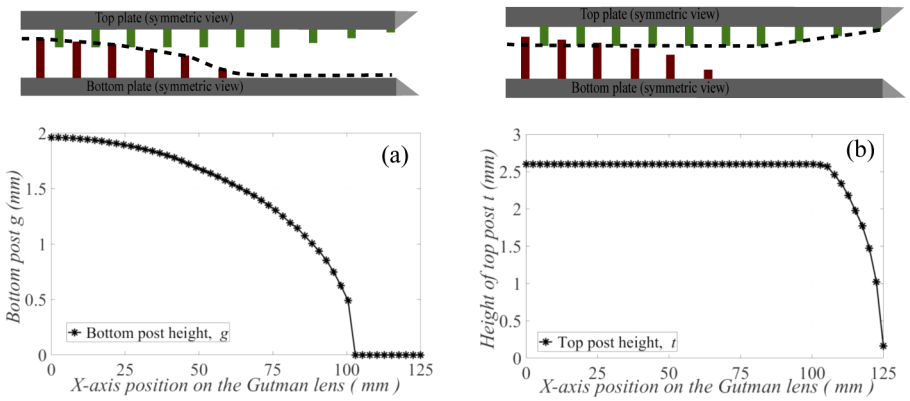

Fig. 10. Metal post heights of the lens along its X axis (a) bottom plate (b) top plate. The height of the metal post correspond to the Z axis of Fig. 9(c).

bottom part are added by mirroring three times the part of Fig. 11(c) to compose the final matrix of Fig. 9(a). The height of the top plate metal posts is calculated with the same methodology where a 2D spline is imported with the data of Fig. 10(b) for the completion of the design of the lens.

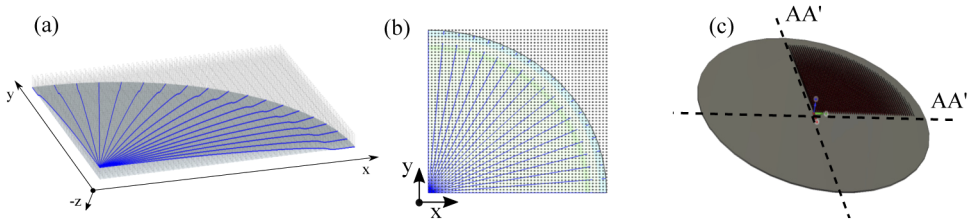

Fig. 11. (a) 3D view of the imported splines over the $K \times K$ matrix of posts of equal heights, (b) 2D splines representation over the $K \times K$ matrix, (c) final modulated metal posts over the bottom metal plate of the PPW.

2.4. Compact feeds

The next challenge that needs to be addressed on the Gutman lens antenna is the selection and the placement of the excitation source along its focal arc. In order to integrate the feeds along the Gutman lens a significant part of the lens needs to be removed. In Fig. 12(a) the surface that has been removed from the lens to integrate the feeds is depicted. Moreover, the focal arc of Gutman lens (red arc) is smaller in comparison with the focal arc of Luneburg (blue arc). It needs to be mentioned that the radii of both Luneburg and Gutman lens are similar and equal to R=125 mm. Thus, compact feeds in a PPW technology that can be integrated along the focal arc of the Gutman need to be examined. Common feeds that have been used to excite a PPW all-metal lens are traditional rectangular waveguides [31] or horn antennas [32]. However, the aperture of a WR75 standard waveguide at Ku-band is equal to 0.79λ and its aperture is very large. One of the goals of this study is to explore compact feeds with small apertures to integrate the maximum amount of feeds along the focal arc of the Gutman which is equal to 6.3λ. The proposed solution is the selection of the single ridge waveguide that is depicted in Fig. 12(b). The compact size of the single ridge is based on the integration of a metal part inside a rectangular waveguide which drops its cut-off frequency. The final single ridge has an aperture of 0.37λ and is twice more

Optics EXPRESS

compact than a rectangular waveguide which has aperture 0.79λ. An example of the comparison of feeds is shown in Fig. 12(b). The focal arc of the Luneburg lens allows the integration of 11 horn antennas while the focal arc of Gutman only 5 horns. The proposed solution of the single ridge waveguide ends up in 12 feeds. The layout of the final demonstrator is depicted in Fig. 12(a). Single ridge waveguide to a microstrip line transformer [33] connected with a 50 ohm SMA connector is finally selected as the final feed. 15 feeds are placed along the focal arc of the lens to complete the design.

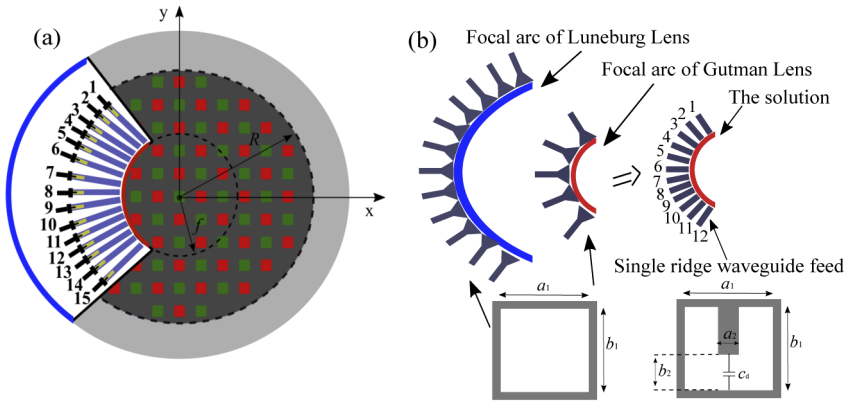

Fig. 12. (a) Layout of the proposed final demonstrator (b) focal arcs of Luneburg and Gutman lens with the integrated feeds.

3. Lens performance

The main advantage of the Gutman lens is the accommodation of the feeds inside the lens which leads to a more compact size lens. This is achieved by removing a part of the original lens. As larger part of the original lens is removed, more compact size and wider field of view can be achieved. However, as larger parts are removed, the performance of the radiation patterns is degraded. This is next demonstrated by studying the radiation patterns as progressively part of lens is extracted. Three separate electromagnetic simulations are actualized using CST Microwave Studio in order to test the broadside patterns at Ku-band while 3 different portions of surfaces are removed from the lens. In Fig. 13(a) a small portion of 7% is removed with arc angle on the periphery of the lens equal to $a = \pi/10$. In Fig. 13(b) a larger portion of 12.4% is removed with arc angle on the periphery of the lens equal to $a = \pi/4$ and in Fig. 13(c) the largest portion of 19% is removed with arc angle on the periphery of the lens equal to $a = \pi/2.6$. In

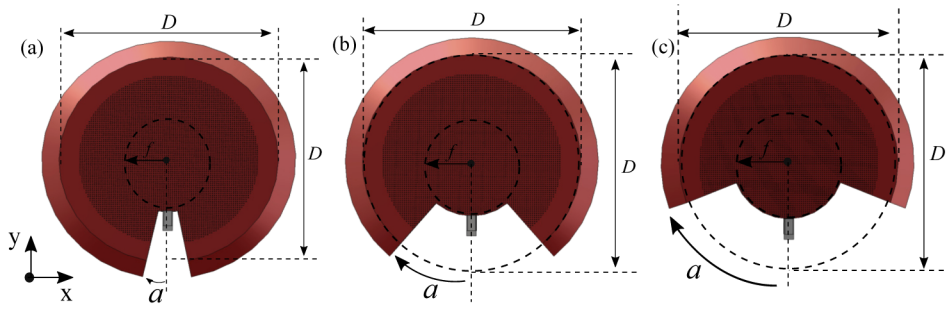

Fig. 13. Broadside beam representation with focal angle (a) $a=\pi/10$ (b) $a=\pi/4$ (c) $a=\pi/2.6$.

Optics EXPRESS

Figs. 14(a)–(c) the E-field is depicted for the broadside beam at center frequency f = 12.5 GHz for these 3 cases. For $a = \pi/10$ and $a = \pi/4$ the spherical wave input of the excitation source is transformed successfully into a plane wave. Moreover, the plane wave that is formed, has a uniform distribution. For $a = \pi/2.6$ the plane wave has aberrations because the highest portion of the lens is removed. The corresponding radiation patterns are depicted in Figs. 15(a)–(c) for the broadside beam for these 3 cases and it is noticed that for $a = \pi/2.6$ the side lobe level (SLL) increases. Considering the performance across the entire Ku-band, higher arc angles results in higher SLL. However, for the broadside beam, the SLL level is under -15 dB for the edge frequency points as well as at the center frequency which is an acceptable value.

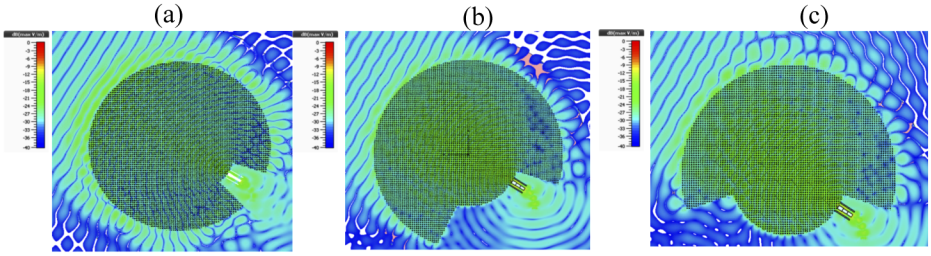

Fig. 14. E-field at center frequency f = 12.5 GHz for the broadside beam with focal angle (a) a=π/10 (b) a=π/4 (c) a=π/2.6.

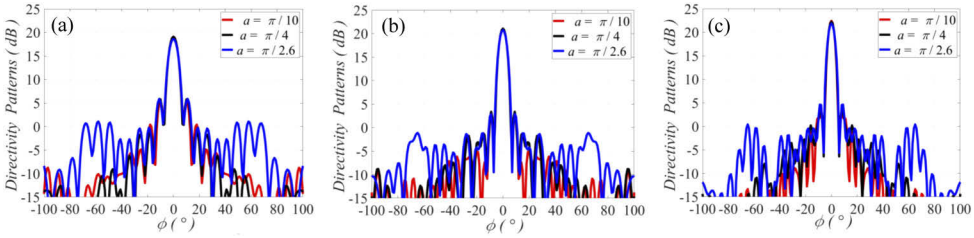

Fig. 15. Radiation patterns for broadside beam of Figs. 13(a)–(c) at Ku-band (a) f = 10 GHz (b) f = 12.5 GHz (c) f = 15 GHz

The same simulation procedure is followed to test the influence of the patterns for one of the extreme beams at −58°. The feed is placed at −60° and 3 separate electromagnetic simulations are realized for $a = \pi/10$, $a = \pi/4$ and $a = \pi/2.6$ (see Figs. 16(a)–(c)). The validation of the scan beam at −58° with maximum value of SLL at -12 dB defined the field of view of the lens at −58°

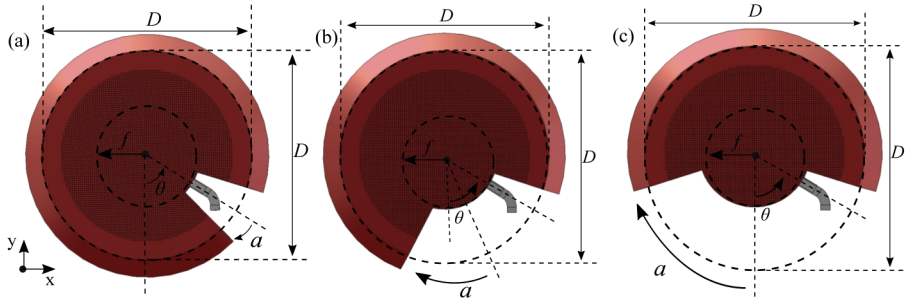

Fig. 16. −58° scan beam representation with focal angle (a) a=π/10 (b) a=π/4 (c) a=π/2.6.

Optics EXPRESS

with maximum scan loss value at 2 dB at the extreme beam. These conclusions can be extracted from the representation of the E-field patterns for the extreme beam at −58° in Figs. 17(a)–(c) as well as from the directivity patterns in Figs. 18(a)–(c). It is noticed from the E-field at center frequency f = 12.5 GHz that for $a = \pi/2.6$ a nearly plane wave is formed for the opposite edge direction of the beam which results to the appearance of side lobes. These side lobes can be seen clearly in Fig. 18(b). Since the rest beams will be placed along the focal arc of the lens for the fixed multi-beam radiation these side lobes will add interference between the main beams, however an SLL value of -12 dB is acceptable. It needs to be mentioned that the pointing angle for the beam at f = 10 GHz and f = 12.5 GHz is −58°, even though the feed is placed on −60°. This shifting in the pointing angle of the beam comes from the slight dispersion of the unit-cell.

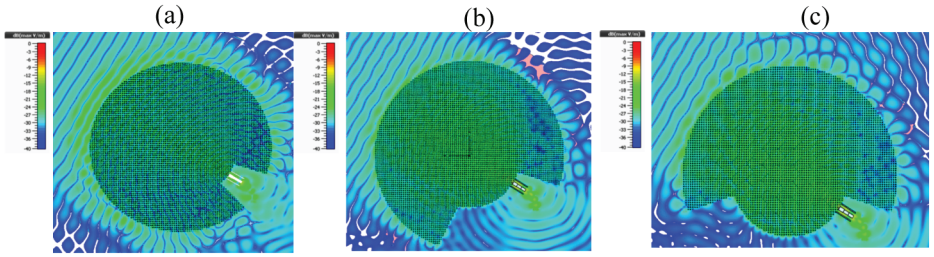

Fig. 17. E-field at center frequency f = 12.5 GHz for −58° scan beam with focal angle (a) a=π/10 (b) a=π/4 (c) a=π/2.6.

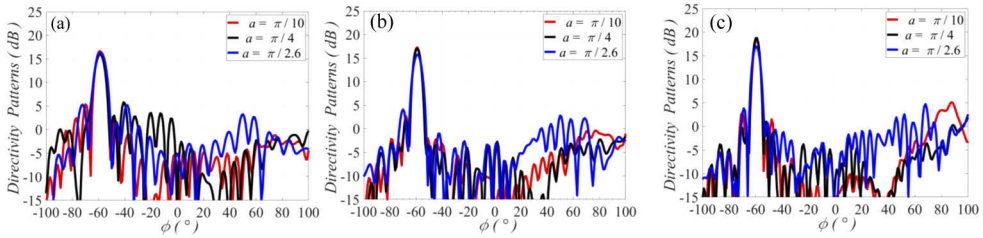

Fig. 18. Radiation patterns for the −58° scan beam of Figs. 16(a)–(c) at Ku-band (a) f = 10 GHz (b) f = 12.5 GHz (c) f = 15 GHz.

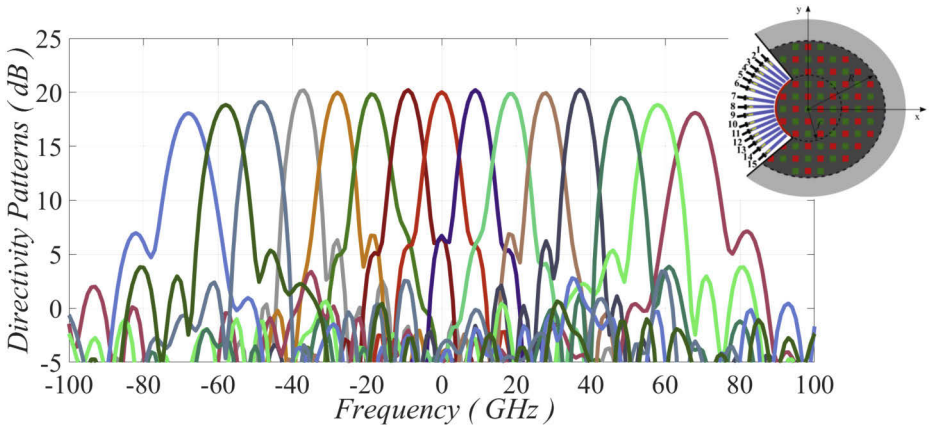

Fig. 19. Directivity patterns at center frequency f = 12.5 GHz.

Optics EXPRESS

Finally, the portion of 19% is removed from the lens in order to create the available area for the placement of the rest feeds as the final demonstrator is a fixed multi-beam system. 15 feeds are placed along the focal arc of the lens (see inset of Fig. 19) and the radiation patterns at the center frequency f = 12.5 GHz are illustrated in Fig. 19. High directive beams are achieved with 3 dB losses and wide field of view up to ±70°. The cross over level is approximately 7° between contiguous beams and for the extreme beam at 70° the SLL equals to -10 dB.

4. Conclusion

In this study, the first graded index Gutman lens utilizing all-metal artificial dielectrics is introduced. The IGS glide symmetry unit-cell is presented and it shows high index value with low dispersion. This artificial dielectric is used to synthesize the lens and a novel design methodology is extensively investigated. Interleaved glide symmetry geometries can open new horizons on the design of periodic structures with high required index values. The radiation performance of the lens is successfully tested and it ended up in the focusing of the input spherical wave source on the periphery of the lens. The present study shows that the Gutman lens exhibits similar radiation performance in comparison with the Luneburg with slightly higher side lobe level. Its compact size is a significant advantage for spacecraft integration since it reduces the mass. Finally, the design of all-metal artificial dielectrics results in low losses and the proposed lens can find applications for satellite missions.

Funding

European Commission (H2020 project REVOLVE, MSCA-ITN-2016-722840).

Disclosures

The authors declare no conflicts of interest.

References

1. R. K. Luneburg, *Mathematical theory of optics* (Brown University, 1944).
2. J. A. Dockrey, M. J. Lockyear, S. J. Berry, S. A. R. Horsley, J. R. Sambles, and A. P. Hibbins, "Thin metamaterial Luneburg lens for surface waves," Phys. Rev. B **87**(12), 125137 (2013).
3. Y. L. Loo, Y. Yang, N. Wang, Y. G. Ma, and C. K. Ong, "Broadband microwave Luneburg lens made of gradient index metamaterials," J. Opt. Soc. Am. A **29**(4), 426–430 (2012).
4. Y.-Y. Zhao, Y.-L. Zhang, M.-L. Zheng, X.-Z. Dong, X.-M. Duan, and Z.-S. Zhao, "Three-dimensional Luneburg lens at optical frequencies," Laser Photonics Rev. **10**(4), 665–672 (2016).
5. S. Tol, F. L. Degertekin, and A. Erturk, "Phononic crystal Luneburg lens for omnidirectional elastic wave focusing and energy harvesting," Appl. Phys. Lett. **111**(1), 013503 (2017).
6. Y. Xie, Y. Fu, and Z. Jia, "Acoustic imaging with metamaterial Luneburg lenses," Sci. Rep. **8**(1), 16188 (2018).
7. A. D. Falco, S. C. Kehr, and U. Leonhardt, "Luneburg lens in silicon photonics," Opt. Express **19**(6), 5156–5162 (2011).
8. C. E. Garcia-Ortiz, R. Cortes, J. E. Gómez-Correa, E. Pisano, J. Fiutowski, D. A. Garcia-Ortiz, V. Ruiz-Cortes, H.-G. Rubahn, and V. Coello, "Plasmonic metasurface Luneburg lens," Photonics Res. **7**(10), 1112–1118 (2019).
9. S. H. Badri and M. M. Gilarlue, "Ultrashort waveguide tapers based on Luneburg lens," J. Opt. **21**(12), 125802 (2019).
10. S. H. Badri and M. M. Gilarlue, "Coupling silica waveguides to photonic crystal waveguides through a multilayered Luneburg lens," J. Opt. Soc. Am. B **37**(1), 104–109 (2020).
11. J. B. Pendry, D. Schurig, and D. R. Smith, "Controlling electromagnetic fields," Science **312**(5781), 1780–1782 (2006).
12. U. Leonhardt, "Optical conformal mapping," Science **312**(5781), 1777–1780 (2006).
13. D. Schurig, J. B. Pendry, and D. R. Smith, "Calculation of material properties and ray tracing in transformation media," Opt. Express **14**(21), 9794–9804 (2006).
14. T. Tyc and U. Leonhardt, "Transmutation of singularities in optical instruments," New J. Phys. **10**(11), 115038 (2008).
15. J. Yi, S. N. Burokur, and A. de Lustrac, "Conceptual design of a beam steering lens through transformation electromagnetics," Opt. Express **23**(10), 12942–12951 (2015).
16. S. Li, Z. Zhang, J. Wang, and X. He, "Design of conformal lens by drilling holes materials using quasi-conformal transformation optics," Opt. Express **22**(21), 25455–25465 (2014).

Optics EXPRESS

17. Z. Chang, X. Zhou, J. Hu, and G. Hu, "Design method for quasi-isotropic transformation materials based on inverse laplace's equation with sliding boundaries," Opt. Express **18**(6), 6089–6096 (2010).
18. N. Landy, N. Kundtz, and D. Smith, "Designing three-dimensional transformation optical media using quasiconformal coordinate transformations," Phys. Rev. Lett. **105**(19), 193902 (2010).
19. H. Ma and T. Cui, "Three-dimensional broadband and broad-angle transformation-optics lens," Nat. Commun. **1**(1), 124 (2010).
20. A. Demetriadou and Y. Hao, "Slim Luneburg lens for antenna applications," Opt. Express **19**(21), 19925–19934 (2011).
21. D. Schurig, "An aberration-free lens with zero F-number," New J. Phys. **10**(11), 115034 (2008).
22. A. S. Gutman, "Modified Luneburg lens," J. Appl. Phys. **25**(7), 855–859 (1954).
23. O. Quevedo-Teruel, W. Tang, and Y. Hao, "Isotropic and nondispersive planar fed Luneburg lens from hamiltonian transformation optics," Opt. Lett. **37**(23), 4850–4852 (2012).
24. O. Björkqvist, O. Zetterström, and O. Quevedo-Teruel, "Additive manufactured dielectric Gutman lens," Electron. Lett. **55**(25), 1318–1320 (2019).
25. N. Memeletzoglou, C. Sanchez-Cabello, F. Pizarro Torres, and E. Rajo-Iglesias, "Analysis of periodic structures made of pins inside a parallel plate waveguide symmetry," Symmetry **11**(4), 582 (2019).
26. W. Yuan, J. F. Chen, C. Zhang, W. X. Tang, L. Wang, Q. Cheng, and T. J. Cui, "Glide-symmetric lens antenna in gap waveguide technology, *IEEE Transactions on Antennas and Propagation* p. 1 (2019).
27. O. Quevedo-Teruel, J. Miao, M. Mattsson, A. Algaba-Brazalez, M. Johansson, and L. Manholm, "Glide-symmetric fully metallic Luneburg lens for 5g communications at ka-band," Antennas Wirel. Propag. Lett. **17**(9), 1588–1592 (2018).
28. K. Liu, F. Ghasemifard, and O. Quevedo-Teruel, "Broadband metasurface Luneburg lens antenna based on glide-symmetric bed of nails," in *2017 11th European Conference on Antennas and Propagation (EUCAP)*, (2017), pp. 358–360.
29. O. Quevedo-Teruel, M. Ebrahimpouri, and M. Ng Mou Kehn, "Ultrawideband metasurface lenses based on off-shifted opposite layers," Antennas Wirel. Propag. Lett. **15**, 484–487 (2016).
30. D. M. Pozar, *Microwave engineering*, 3rd Edition (Wiley, 2005).
31. H. Lu, Z. Liu, Y. Liu, H. Ni, and X. Lv, "Compact air-filled Luneburg lens antennas based on almost-parallel plate waveguide loaded with equal-sized metallic posts," IEEE Trans. Antennas Propag. **67**(11), 6829–6838 (2019).
32. C. D. Diallo, E. Girard, H. Legay, and R. Sauleau, "All-metal ku-band Luneburg lens antenna based on variable parallel plate spacing fakir bed of nails," in *2017 11th European Conference on Antennas and Propagation (EUCAP)*, (2017), pp. 1401–1404.
33. H.-W. Yao, A. Abdelmonem, J.-F. Liang, and K. A. Zaki, "Analysis and design of microstrip-to-waveguide transitions," IEEE Trans. Microwave Theory Tech. **42**(12), 2371–2380 (1994).